Corrosion behavior of iron plates in cementitious solution at 80°C in anaerobic conditions

David Pally, Patrick Le Bescop, Michel Schlegel, Frédéric Miserque, Laure Chomat, Delphine D. Neff, Valérie L'Hostis

Corrosion behavior of iron plates in cementitious solution at 80°C in anaerobic conditions

David Pally [a], Patrick Le Bescop [a], Michel L. Schlegel [b], Frédéric Miserque [c], Laure Chomat [a], Delphine Neff [d], Valérie L'Hostis [e],

[a] *Des – Service d'Etude du Comportement des Radionucléides (SECR), CEA, Université Paris-Saclay, F-91191, Gif-sur-Yvette, France*
[b] *Des – Service d'Etudes Analytiques et de Réactivité des Surfaces (SEARS), CEA, Université Paris-Saclay, F-91191, Gif-sur-Yvette, France*
[c] *Des – Service de Corrosion et de Comportement des Radionucléides dans leur Environnement (SCCME), CEA, Université Paris-Saclay, F-91191, Gif-sur-Yvette, France*
[d] *LAPA-IRAMAT, NIMBE, CEA, CNRS, Université Paris Saclay, CEA Saclay, F-91191, Gif-sur-Yvette, France*
[e] *Des – Département de Physico-Chimie (DPC) CEA, Université Paris-Saclay, F-91191, Gif-sur-Yvette, France*

Abstract

Iron was corroded in anoxic cementitious (pH 13.2) media (filtered porewater or cement slurry) at 80°C; corrosion products were investigated by microscopic techniques. A thin film of magnetite (Fe_3O_4) formed during the first immersion days. For longer immersion times (90 days) in cement slurry, hydroandradite (HA) ($Ca_3(Fe^{3+})_2(SiO_4)_y(OH)_{4(3-y)}$) formed a dense outer layer and an heterogeneous inner layer. A thin oxide layer is always observed in contact with metal and is believed to correspond to a protective barrier. Our results suggest that in the conditions of the Belgian Supercontainer for radioactive waste disposal, a passive layer can form slowing down corrosion.

Keywords : Iron; concrete; Alkaline corrosion; magnetite; hydroandradite; barrier layer

1 Introduction

The Belgian reference for high-level radioactive waste packaging proposed by the Belgian Agency for Radioactive Waste and Enriched Fissile Materials (ONDRAF/NIRAS) is called supercontainer [1]. This concept includes a stainless steel liner, a concrete buffer and a carbon steel overpack containing one or several waste canisters. The purpose of the concrete buffer is to maintain high alkaline conditions on the surface of the overpack, thus keeping the steel surface in the so-called "passivation" range of pH. The supercontainer will be emplaced in the Boom clay, a rock formation saturated with low-chloride (100 ppm) porewater. During the first tens of thousands of years, the overpack will be exposed to the concrete alkaline porewater in the concrete buffer [2]. After a relative short period of oxygen removal by aerobic corrosion and microbial activity, the steel interface will experience anoxic conditions [3]. Eventually, the ingress of chloride from Boom clay to the overpack could not be excluded. The chloride aggressiveness with respect to the overpack would depend on a corrosion layer previously developed in an anoxic alkaline environment, and enriched in Si, Ca and Al. Therefore, understanding steel corrosion in alkaline porewater in contact with cement material, in anoxic media, and at 80°C, is essential to predict the long-term integrity of the supercontainer.

Corrosion and long-term behavior studies in concrete-based environments were performed either in synthetic pore solutions [4-8], or in bulk cementitious matrices [9-11]. Experiments of metal iron or steel corrosion in fresh concrete matrices generally resulted in slow corrosion rates, explained by the low solubility of Fe oxides in alkaline conditions [12, 13]. However, these experiments were usually performed in aerated environments to investigate the impact of parameters such as diffusion of gas from the atmosphere, of chloride after immersion in synthetic seawater, of rainwater, or the impact of cracks. Corrosion monitoring was performed by electrochemistry [12, 14], weight loss measurements [15, 16], or by monitoring the pressure increase due to hydrogen evolution under anoxic conditions [17]. A number of corrosion experiments were also performed in pure solution, in order to investigate the electrochemical behavior at iron or steel surface. Usually these experiments were performed in a saturated solution of portlandite ($Ca(OH)_2$) [14, 18-20], sometimes with addition of chemical elements or salts. For example, gypsum ($CaSO_4$) [5, 21] or NaCl [22-26] were added to assess the impact of

52 sulfate and chloride, respectively. A third type of experiment was performed in porewater equilibrated
53 with a prepared cement grout [27]. Such a solution would contain all of the elements in (pseudo)-
54 equilibrium with respect to cement phases. However, these studies were performed at ambient to
55 moderate (≤ 50°C) temperatures, significantly lower than the reference temperature of the repository
56 thermal peak (about 80°C).

57 Corrosion of iron, and, by reference, carbon steel, in highly alkaline environments (pH > 13) is expected
58 to result in the formation of a duplex interface made of two distinct layers. The inner layer grows into
59 the metal, and the outer layer grows towards the environment by precipitating solution elements [28,
60 29]. Several models were developed to account for the growth of this duplex interface, such as e.g. the
61 Point defect model [30, 31], the mixed conduction model [32], or the Diffusion Poisson Coupled Model
62 (DPCM) [33]. Most of these modelling efforts focused on the formation of an inner film, believed to be
63 responsible for surface passivation. However, the outer layer is expected to hinder corrosion by limiting
64 the flux of chloride ions to the metal surface. Thus the duplex interface is expected to play a key role in
65 the sensitivity of the passive layer to pitting corrosion.

66 The goal of the present study is to assess iron corrosion in a concrete environment at 80°C under anoxic
67 conditions representative of a deep geologic repository. Metal samples were corroded in a concrete
68 synthetic solution, in the presence of cement powder (CEM I) in order to provide a steady source of
69 dissolved elements (such as Ca, Si) in (pseudo-)equilibrium with cement phases. Two types of samples
70 were investigated. First, iron powder with a high specific surface area was used to reveal the impact of
71 cement presence on corrosion by monitoring the rate of hydrogen evolution. Second, rolled or polished
72 plates of iron were used to identify the corrosion products and place constraints on the corrosion
73 mechanism. The corrosion interface was characterized by techniques such as micro-Raman (μRaman)
74 spectroscopy, X-Ray Diffraction (XRD), Scanning Electron Microscopy (SEM), X-ray photoelectron
75 spectroscopy (XPS) and Scanning Transmission X-ray Microscopy (STXM). These characterizations
76 shed light on the nature of the corrosion interface and help pinpoint the passivating properties to specific
77 features of the corrosion layers.

78

2 Materials and methods

2.1 Materials

The filler was made using CEM I 42,5 cement (Dannes factory). The cement mineralogy (obtained by Rietveld analysis of a powder X-ray diffractogramm) and composition are given in Table 1. The composition of the filler was taken from the formulation elaborated by ONDRAF/NIRAS for the material in contact with the overpack. One liter of cement paste was made with 514.8 g of CEM I 42,5 cement (Dannes factory), 876.3 g of 2001M filler calcite, and 514.8 g of water. The pore solution is obtained by pressing (to 450 MPa) samples after 28 days of hydration at 20°C or 80°C using a mechanical press. The solution is analyzed by Inductively Coupled Plasma Atomic Emission Spectroscopy (ICP-AES). Table 2 shows the composition of the sampled pore solution. At room temperature, the sulphur concentration is driven by the ettringite solubility. The relatively high concentration measured at 80°C is associated to the total dissolution of ettringite.

Table 1: Composition of the CEM I 42,5 cement (Dannes factory).

Chemical composition										
Compounds	CaO	SiO_2	Al_2O_3	Fe_2O_3	MgO	Na2O	K_2O	Na_2O.eq	SO_3	Cl^-
(Wt %)	64.6	21.3	4.0	5.4	1.0	0.15	0.55	0.51	1.6	0.01

Mineralogical composition [a]					
Phase Content	C2S	C3S	C3A	C4AF	Anhydrite
(Wt %)	27.5	51.9	0.3	18.3	2.0

[a] Obtained by Rietveld analysis of a powder X-ray diffractogram.

Table 2: pH and concentration of dissolved elements in the pore solution sampled after 28 days of hydration.

	20°C	80°C[a]
pH (measured at 21°C)	13.2	
$[Al]_{aq}$ (mmol/L)	< 0.04	< 0.04
$[S]_{aq}$ (mmol/L)	0.36	18.8
$[Si]_{aq}$ (mmol/L)	0.044	0.05
$[Ca]_{aq}$ (mmol/L)	4.6	3.9
$[Na]_{aq}$ (mmol/L)	60	63
$[K]_{aq}$ (mmol/L)	145	139

Corrosion experiments were performed on iron powders and plates. Iron powder (Goodfellow, diameter 6 µm) was used in order to maximize the specific surface area and hydrogen evolution during the corrosion process. Iron plates were used to investigate the nature of the corrosion interface. They were of two distinct origins and surface preparations. Armco iron plates (composition in Table 3; [34]) of 2 mm thickness were polished with SiC abrasive papers (Presi, Mecaprex) and absolute ethanol (Fluka). Diamonds pastes of 3 and 1 µm were used for final polishing under ethanol. Rolled plates of pure iron (Goodfellow) with a thickness of 0.5 mm were ultrasonically degreased in ethanol prior to use.

Table 3. Chemical composition of the pure iron (Armco).

Element	C	Si	Mn	S	P	Cu	Fe
Wt.%	0.002	0.009	0.33	0.019	0.005	0.03	Base

2.2 Experimental setup

All solution and sample preparations were performed in an anoxic glove box to avoid oxygen. Specific setups for plate corrosion were designed to reproduce the anoxic environment and relatively high temperature (80°C) expected at the overpack surface in the supercontainer system (Figure 1). Iron exposure to the cementitious environment was performed under either static or stirred conditions (Table 4). For static experiments (no stirring), the system was made by a stainless steel reactor connected to a pressure sensor with a Swalegok® tube and containing iron powder and plates. Iron plates were positioned on a polytetrafluoroethylene (PTFE) support structure to avoid any contact between each plate (Figure 1a). The temperature was fixed by immersing the reactor in a thermostatic water bath (Figure 1b). For dynamic experiments (stirring), the system contained only iron powder. It was heated by a heating ring and stirred with a blade (Figure 1c,d). A Teflon jar was added in all experiments to

avoid any galvanic interactions between iron powder and the stainless steel reactor. The pressure was measured with a Keller Record digital pressure sensor (measurement range: -1 to 30 bar; automatic recording). During corrosion, the reaction pots were hermetically sealed and heated at 80°C.

For experiments with iron powder only and cement phases (hereafter identified by GPC for "Goodfellow® Powder – Cement"), chemical conditions in the concrete buffer were reproduced by mixing cement material (hydrated CEM I 42.5, Dannes) and alkali solution (63 mmol/L NaOH, at 139 mmol/L KOH). The slurry was heated during one week at 80°C, and then iron powder was introduced. The reactor was hermetically sealed, placed in the thermostatic water bath, and reacted for 42 days (GPC) at 80°C. For experiments on iron powder in absence of solid CEM I phase (GPWoutC), the slurry was filtered and iron was introduced in the synthetic porewater solution and corroded for 64 days at 80°C in the water bath. For experiments with iron powder and plates, polished plates were corroded for 4, 10 or 90 days, and rolled plates for 20, 39 and 160 days (Table 4). Hydrogen evolution was monitored by measuring the increase in total pressure of the reaction vessel. Gas samples were collected at the end of the experiments, and analyzed by mass spectrometry (MAT 271, Thermo/Finnigan) to confirm the final amount of evolved H_2.

After corrosion, coupons or powders (separated from the cement with an electromagnet) were rinsed with ethanol, dried and stocked in glove box in N_2 atmosphere. Table 4 lists all samples analyzed in this study and the related preparation conditions.

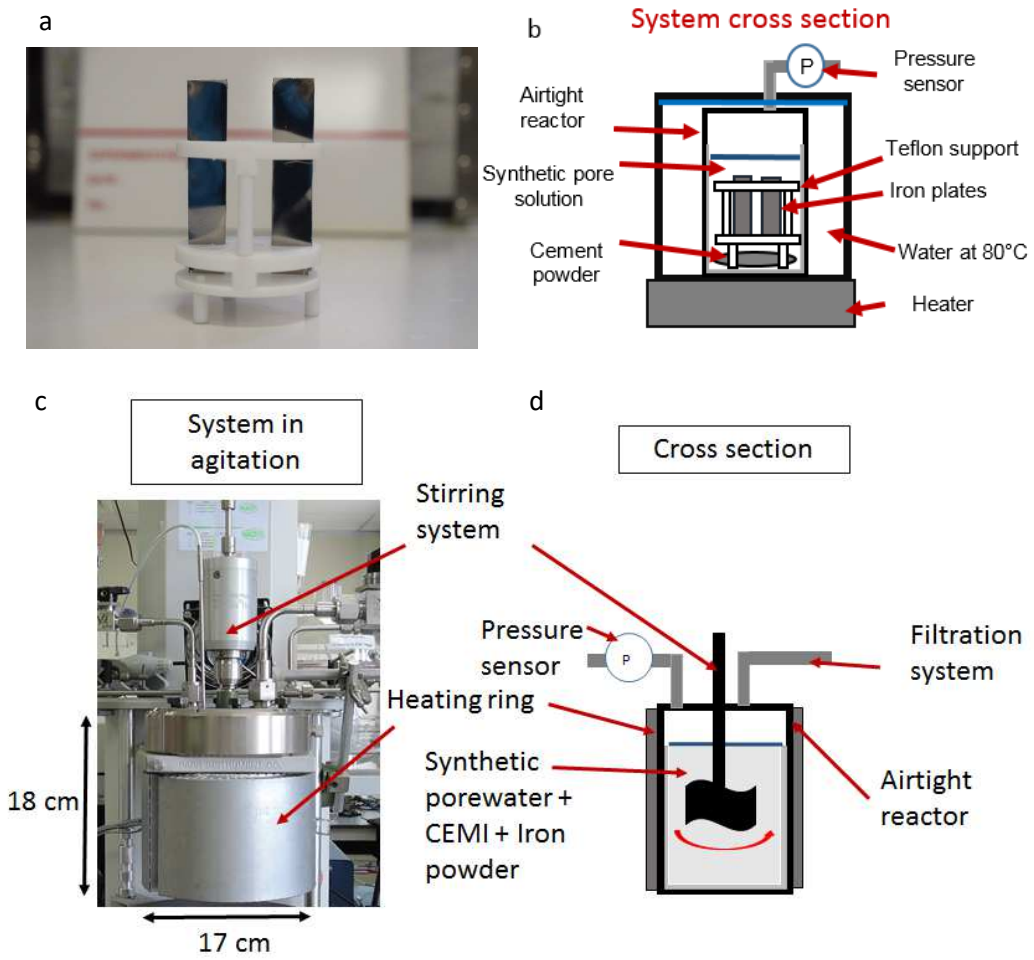

Figure 1. (a) Support for iron plates in unstirred corrosion experiments. (b) Schematic illustration of the corrosion setup of static corrosion in anoxic environment. (c,d) Photography and schematic illustration of the corrosion setup with stirring capabilities.

Table 4. List of samples investigated in this study

Sample name	Iron form	Preparation	Iron mass (g)	Cement mass (g)	Solution volume (mL)	Reaction time (d)	Stirred
APP_0	Powder + plate	Polished 1 µm	/	/	/	0	/
APP_4	Powder + plate	Polished 1 µm	1.2 + 28.1	37	140	4	no
APP_10	Powder + plate	Polished 1 µm	1.2 + 33.7	37	140	10	no
APP_90	Powder + plate	Polished 1 µm	1.2 + 30.1	37	140	90	no
GLP_0	Powder + plate	Rolled	/	/	/	0	/
GLP_20	Powder + plate	Rolled	1.2 + 28.8	37	140	20	no
GLP_39	Powder + plate	Rolled	1.2 + 50.6	37	140	39	no
GLP_160	Powder + plate	Rolled	1.2 + 37.7	37	140	160	no
GPC	Powder (∅ 6 µm)	/	18.72	37	305.25	42	yes
GPWoutC	Powder (∅ 6 µm)	/	17.2	0	621.14	64	yes

2.3 Microstructural characterization

The powder samples (GPC, GPWoutC) and corroded plates were characterized by XRD immediately after being taken out of the glove box to limit oxidation of the corrosion layers. X-Ray Diffraction data for powders and plates were collected in the Bragg-Bentano geometry using a PANalytical X'Pert diffractometer with an X'Celerator detector (CuK_α, λ = 1.5405 Å). The reciprocal space was scanned between 5° and 60°2θ with a step size of 0.016°2θ.

Micro-Raman investigations were performed using a Horiba-Jobin Yvon X'Plora spectrometer, with an excitation wavelength of 532 nm, and microanalyses were performed with a long-range 50× objective (Olympus), with a lateral resolution of about 5 µm. The laser beam was filtered at 10 % of the nominal power to prevent the potential thermal degradation of sensitive Fe phases [35].

For SEM, the surface of sample plates were analyzed without prior preparation. The samples were quickly transferred (< 1 min) in the microscope (Zeiss EVO MA 15) and kept under vacuum. An accelerating voltage of 15 kV was used. The working distance was approximatively 10 mm and the beam current was fixed at 100 nA. The Energy dispersive X-ray (EDX) spectra were collected with a Bruker detector associated with ESPRIT software.

Analyses by XPS were carried out with a Thermofisher Escalab 250 XI spectrometer using a monochromatic Al K_α X-Ray source (1486.6 eV) [10]. The samples were introduced in the spectrometer using a connected N_2 atmosphere glove box. The spot size diameter for classical analysis was 900 µm. The spectrometer was calibrated to the silver Fermi level (0 eV) and to the $3d_{5/2}$ core level of metallic silver (368.3 eV). The following core levels were recorded with a 20 eV pass energy: Fe-2p, Ca-2p, O-1s, C-1s, Si-2p. Data processing was performed using the commercial Avantage® software (ThermoFisher Scientific Inc.). The Shirley background subtraction method was used for the fitting procedure.

Thin sections of corrosion interface were extracted from the corroded plates by Focused Ion Beam (FIB), using a Nanolab 660 (FEI) equipped with a Ga^+ ion source and an EDXS Oxford detector for Energy Dispersive X-ray spectroscopy (EDXS). The plates were first coated with a thin carbon conducing film,

and then a Pt strip was deposited directly on the corrosion outer surface. The thin film was excavated and thinned to about 100 nm following a standard procedure [36]. Scanning transmission electron microscopy (STEM) images and EDXS data were collected on the samples at an acceleration voltage of 30 kV using the scanning transmission detector.

The STXM experiments were performed at the 10ID-1 beamline of the Canadian Light Source (CLS, Saskatoon), which has a focused beam of 30 nm in diameter [37]. Sequences (stacks) of images were collected on selected areas at X-ray energies near the Fe L_3-edge (709 eV). The energy range ([700,760 eV]) and the scan resolution (0.15 eV at the Fe L_3-edge) were selected to obtain a good compromise between total acquisition time (each image was collected within about 0.5-1 min, and each stack of 130 to 180 images within 1-2 h) and spectral resolution [37, 38]. The measured transmitted signals (I_t) were converted into absorbance values using the incident flux (I_0) measured in the absence of X-ray absorption. Reference spectra were collected under the same conditions [39, 40]. The intensity of the reference spectra was normalized to obtain an absolute linear absorbance scale (i.e., absorbance per unit path length of a pure material with a known density) using the computed elemental response outside the structured near-edge region [41] and the density of the material [40, 42]. Singular Value Decomposition (SVD) was used to obtain quantitative maps from the Fe L-edge stacks in terms of the respective contributions in $Fe^{(0)}$, $Fe^{(II)}$ and $Fe^{(III)}$, using aXis2000 [38-40]. The $Fe^{(0)}$, $Fe^{(II)}$ and $Fe^{(III)}$ contributions were modeled using the spectra of pure ferrite, siderite ($Fe^{(II)}CO_3$), and maghemite ($Fe^{(III)}{}_2O_3$) references, respectively [38, 39, 43]. This fitting procedure allows quantifying the relative proportion of Fe oxidation states phases in the sample with a good precision (a few per cent). Finally, the uniqueness of the solution was assessed using a multiple linear regression curve-fitting procedure.

3 Results

3.1 Corrosion of iron powder

The important surface area of the iron powder makes it possible to monitor hydrogen evolution with measurable amounts. Figure 2 compares the amount of evolved dihydrogen in a CEM I slurry (GPC), and in a pure cementitious solution without CEM I particles (GPWoutC). It is evident that the presence

of solid cement phases is extremely important, as hydrogen evolution for GPC is significant from the first day of reaction. However, hydrogen evolution significantly slows down after about 15 days of reaction. In contrast, hydrogen evolution is significantly slower during the first 10 days for GPWoutC. It then accelerates for 10 days, and eventually reaches a plateau after a total reaction time of 20 days. This simple experiment demonstrates that hydrogen evolution, and, by inference, corrosion rate, are significantly enhanced by the presence of cement material.

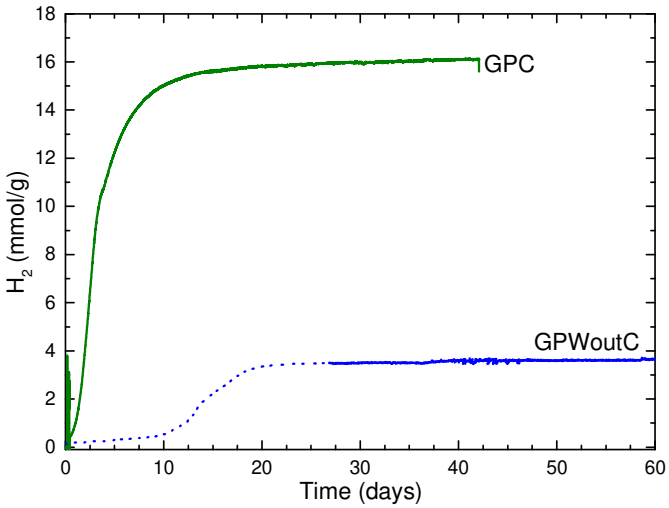

Figure 2. Amounts of dihydrogen produced during the corrosion of iron powder in cementitious slurry or solution at 80°C. Green solid: GPC; blue dotted: GPWoutC.

Characterization of the corroded powders by XRD (Figure 3) shows that only a weak contribution from magnetite could be detected for GPWoutC. In contrast, for GPC, additional diffraction peaks are visible. Most of these peaks can be attributed to andradite grossular hydrogarnet (AGH) [44]. The nominal composition of AGH is $Ca_3AlFe(SiO_4)(OH)_8$, but similar compounds with slightly different compositions ($Ca_3(Al_xFe_{1-x})_2(SiO_4)_y(OH)_{4(3-y)}$ with $0 < x < 1$ and $0 < y < 2$) can lead to small but significant shifts in the position of XRD peaks between 10° and 35° [45]. In our case, the peak positions seem to coincide with the compound for which $y = 1$ and $x = 0$ (i.e. $Ca_3Fe^{(III)}_2(SiO_4)(OH)_8$), corresponding to hydroandradite (HA) (ICSD file 29247; [46]). Additional XRD peaks are attributed to calcite, probably resulting from the carbonation of the cementitious paste that was incompletely separated from the iron powder.

In conclusion, both the magnitude of hydrogen evolution and the contrasted composition of the reacted solids demonstrate that corrosion mechanisms strongly depend on the presence of cement phases. The morphology and composition of the corrosion interfaces will be detailed in the next section.

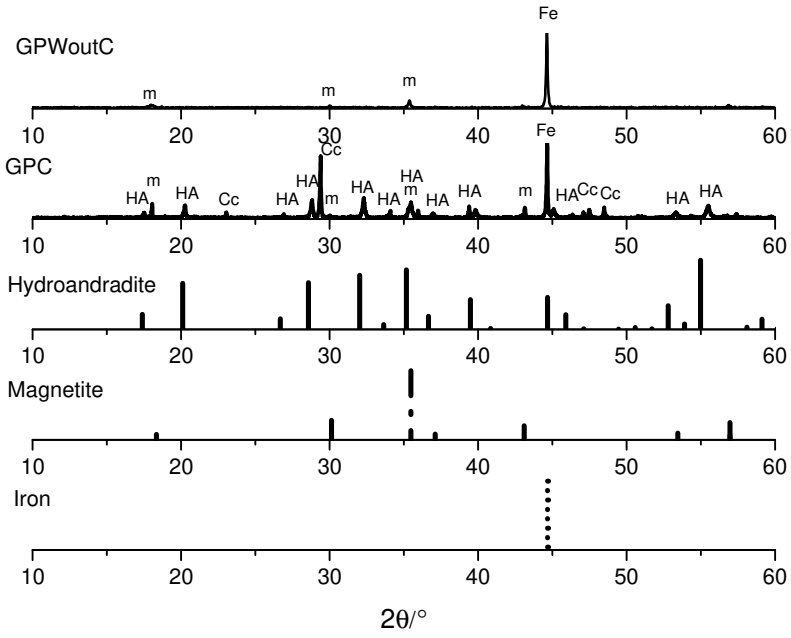

Figure 3. XRD diagram of iron powders after corrosion with (GPC) or without (GPWoutC) cement materials during the corrosion in solutions at 80°C. Peaks are assigned to hydroandradite (HA; ICSD 29247), to magnetite (m; ICDD 01-071-4918), to iron (Fe; ICDD 00-006-0696), and to Ca carbonate (Cc; ICDD 00-001-0586).

3.2 Corrosion of iron plates

3.2.1 Morphology and chemical composition of corrosion layer

Figure 4 shows the evolution of the plate surfaces as a function of reaction time as observed by SEM in BackScattered Electron (BSE) mode. For the polished plates, the initial surface is smooth, with only a few polishing scratches (Figure 4a). After 4 days of reaction (APP_4; Figure 4b), the surface seems to be slightly roughened, and round particles of about 1 µm in diameter were observed. The EDX signal from the slightly roughened surface (PI 2; Figure 4b and Table 5) is dominated by Fe, with a very weak O contribution (2.4 at.%). Thus, if a surface layer of oxide is present, it is very thin. Analysis of the isolated particles by EDX detects Ca (8.6 at.%), Si (1.2 at.%), O (35.3 at.%), and Fe (54.7 at.%), hinting

227 at the formation of solids containing these elements. The strong Fe contribution may also result from
228 the spillover of the electron beam, resulting in a significant contribution from the iron substrate.

229 The iron surface becomes significantly heterogeneous after 10 days of immersion (Figure 4c), with two
230 distinct types of areas. First, some areas seem to be smooth and hardly affected by corrosion. Indeed
231 EDX analysis shows that the O content in these layers (9.5 at.%), although significantly larger than for
232 unreacted iron, is still much lower than expected for an oxide layer (PI 4; Figure 4c and Table 5). Other
233 areas are covered by octahedral crystals made of Ca, Si, Fe and O (PI 5; Figure 4c and Table 5). These
234 crystals cover the entire surface after 90 days of reaction, and their composition is dominated by Ca, Fe,
235 Si, and O (PI 6; Figure 4d and Table 5), in proportions similar to the composition obtained after 10 days
236 of reaction.

237 Compared to the polished surface of APP_0, the surface of GLP_0 exhibits oriented marks typical of
238 rolling (Figure 4e). After 20 days of reaction, most of the surface is covered by euhedral crystals made
239 of Fe, O, Ca, and Si (Figure 4f, PI 8), together with areas covered by small crystallites, with an EDX
240 signal dominated by iron (PI 9). These smooth areas decrease in proportion for GLP_39 (Figure 4g).
241 After 160 days of reaction, the plate is fully covered by a dense layer of euhedral particles (Figure 4h).
242 The chemical composition is dominated by Ca, Si, Fe, and O (PI 12). Incidentally, the relative
243 composition of these PI is in fair agreement with a $Ca_3Fe_2Si_{1.15}O_{4.6}(OH)_{7.4}$ composition of HA [46]. This
244 coincidence strongly suggests that the euhedral particles are essentially made of HA.

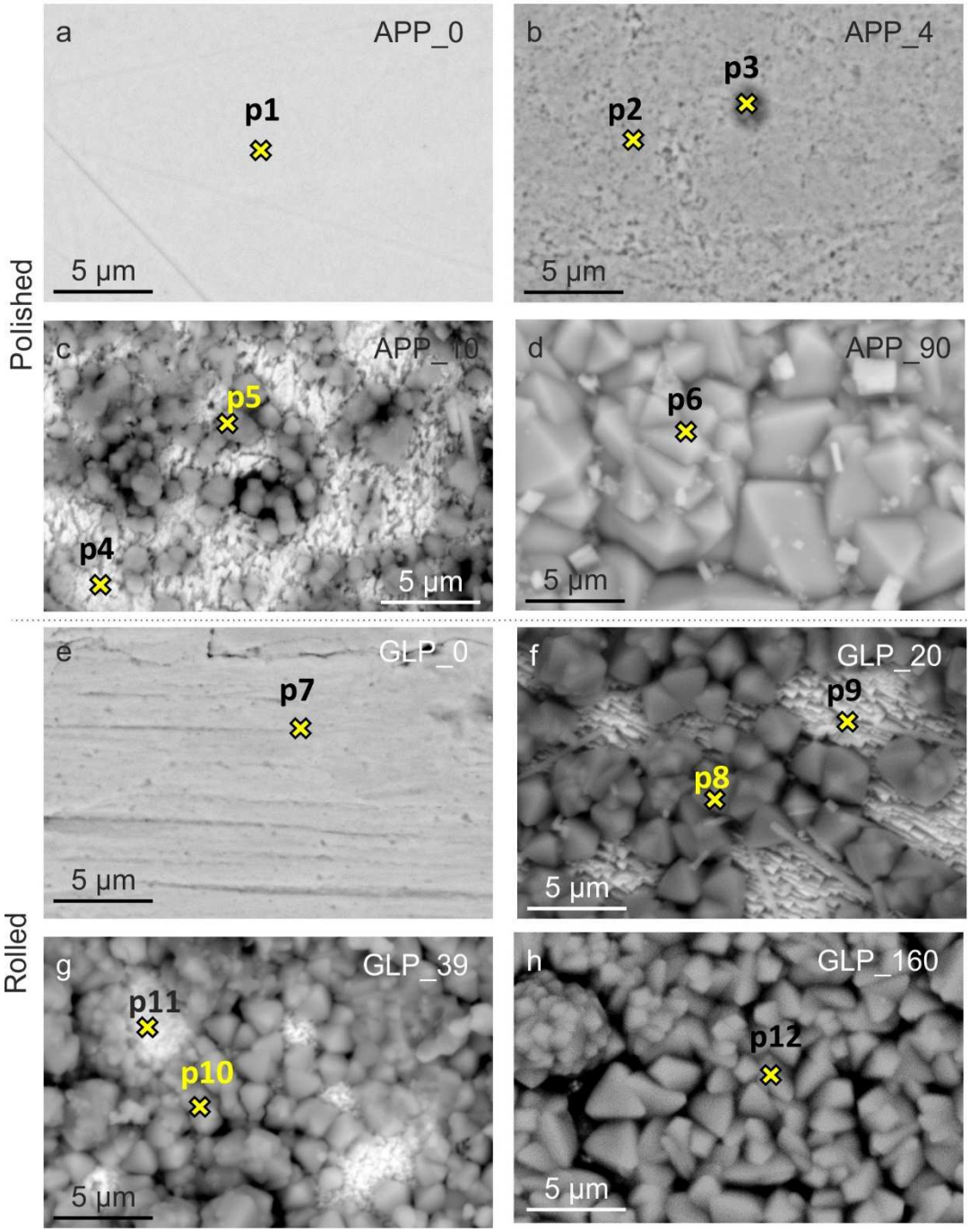

Figure 4. SEM-Backscattered electron (BSE) images (magnification 5000×) obtained on iron polished (a-d) or rolled (e-h) plates corroded in the porewater slurry. (a) APP_0, (b) APP_4, (c) APP_10, (d) APP_90, and rolled plates (e) GLP_0, (f) GLP_20, (g) GLP_39, (h) GLP_160.

Table 5. Quantitative analysis by EDXS of selected points of interest (PI) at the corrosion interface. Analysed points are located on the images of Figure 4.

Sample	PI	Composition (at. %)				
		O	Al	Si	Ca	Fe
APP_0	PI 1	1.1	-	-	-	98.4
APP_4	PI 2	2.4	-	0.3	-	97.0
	PI 3	35.3	-	1.2	8.6	54.7
APP_10	PI 4	9.4	-	0.6	1.5	88.5
	PI 5	**68.4**	**1**	**4.6**	**13.8**	**12.2**
APP_90	PI 6	**65**	**0.3**	**6.4**	**17.4**	**10**
GLP_0	PI 7	2.14	0.15	0	0.2	97.5
GLP_20	PI 8	**68.5**	**0.5**	**5.3**	**15**	**10.7**
	PI 9	9.5	0.3	0.5	1.2	88.5
GLP_39	PI 10	**65.3**	**0.4**	**5.9**	**17.3**	**11.2**
	PI 11	23.3	0.5	2.9	5.4	68
GLP_160	PI 12	**65.3**	**1**	**6.2**	**18**	**9.5**
HA[a]		**66.1**	**0**	**6.3**	**16.5**	**11**

[a] Hypothetical composition calculated from the $Ca_3Fe_2Si_{1.15}O_{4.6}(OH)_{7.4}$ [46].

3.2.2 Structural characterization of corrosion layers

3.2.2.1 XPS

The surface of the corroded plates were characterized first by XPS, a relevant technique to study the type of passive films formed in cementitious solutions [14, 47]. The XPS survey spectra of the different samples show that the plate surfaces are mostly composed of Ca, Si, Fe and O (Figure 5). Figure 6 shows the spectra at the binding energy range of Fe-$2p_{3/2}$ core level. For the iron plate immersed during 4 days, the Fe $2p_{3/2}$ core level is fitted using three contributions. The narrow and asymmetric components at 706.7 ± 0.3 eV is characteristic of metallic iron ($Fe^{(0)}$). The detection of $Fe^{(0)}$ at this immersion time shows that the Fe oxide layer is very thin (less than 10 nm) or heterogeneous (coexisting with bare metal). The contributions at 708.9 ± 0.3 eV and 710.7 ± 0.3 eV are attributed to Fe oxide with Fe at oxidations states of +II ($Fe^{(II)}$) and +III ($Fe^{(III)}$), respectively. The general envelopes for these Fe chemical contributions can be built using peaks corresponding to the "Gupta and Sen" multiplets [48, 49]. The corresponding multipeak parameters were provided by Grosvenor *et al.* [50] who investigated the multiplet splitting of Fe-*2p* XPS spectra for Fe compounds. This fitting processing has been recently used for characterization of Fe_3O_4 deposits: the presence of both $Fe^{(III)}$ and $Fe^{(II)}$ is suggestive of magnetite [51]. The resulting $Fe^{(III)}/Fe^{(II)}$ ratio is found to be approximately of 2.2:1 which is close to the expected theoretical ratio of 2:1 ($Fe^{(III)}_2Fe^{(II)}O_4$). The $Fe^{(II)}$ and $Fe^{(III)}$ contributions are still observed for

APP_10 (Figure 6), but the $Fe^{(0)}$ contribution is no longer present, probably buried under a thicker corrosion layer. The $Fe^{(III)}/Fe^{(II)}$ ratio increases to 7.3/1 due to oxidation of the outer layer. For the plates immersed for 90 days (APP_90 and GLP_160), a chemical shift of the binding energy is observed, and the $Fe^{(III)}$ contribution appears at 712.0 ± 0.3 eV. This binding energy can be attributed to $Fe^{(III)}$ in a silicate chemical environment [52, 53].

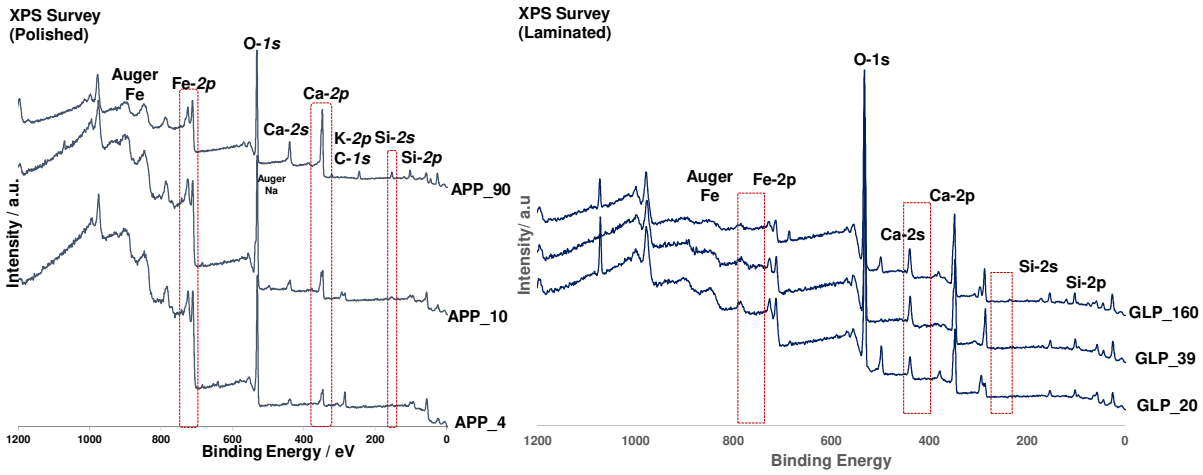

Figure 5. XPS Survey of polished plates corrode during 4, 10 and 90 days (left) and rolled plates reacted for 20, 39 and 160 days (right).

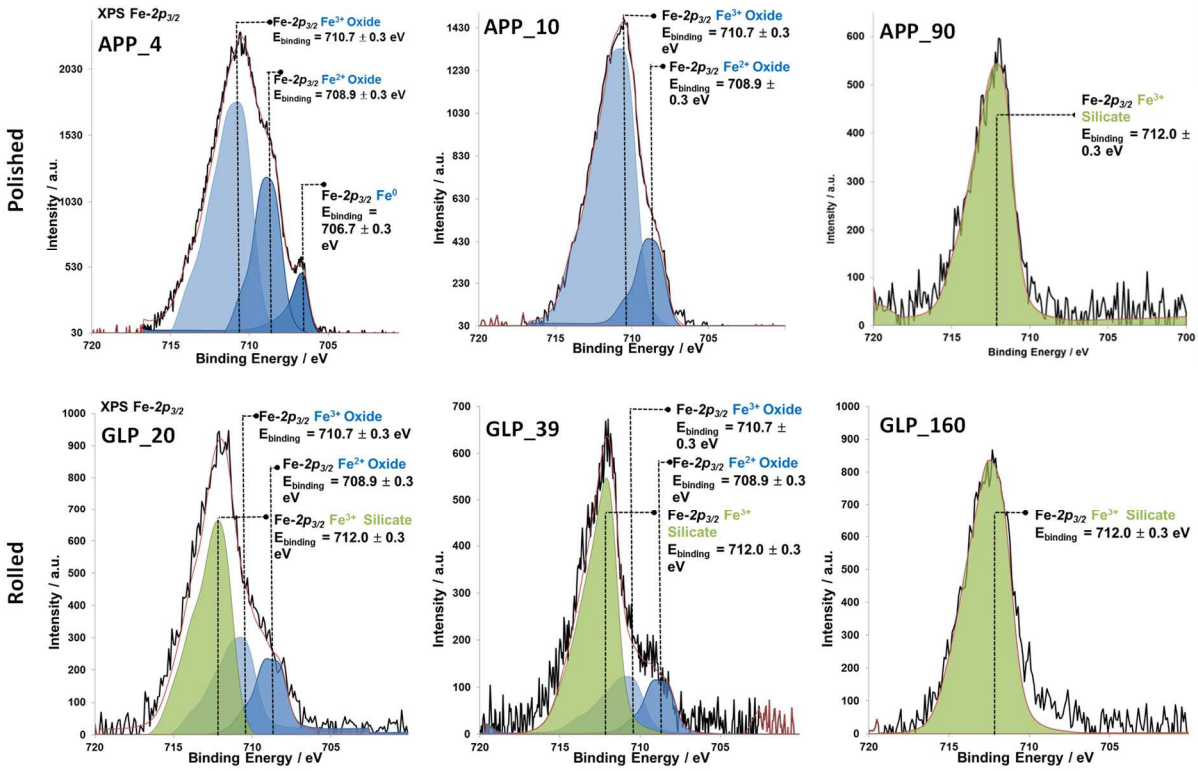

Figure 6. Fe $2p_{3/2}$ core level XPS spectra of iron plate rolled or polished immerged for 4, 10, 20, 39, 90 and 160 days in cementitious solution at 80°C (after Shirley background subtraction). Blue colors refer to contributions from magnetite and metal Fe, green to contributions from HA.

3.2.2.2 XRD

Figure 7 shows that the XRD diffractograms for rolled or polished plates are similar. Only the Fe peak related to the iron plate is visible for short immersion times (APP_4). This observation shows that the corrosion layer is too thin to be detected by XRD. Afterwards, additional peaks attributed to HA appear, and their intensity increases with immersion time (APP_10, APP_90, GLP_20, GLP_39, and GLP_160), indicating accumulation of this solid. Magnetite is also detected for reaction times greater than 90 days.

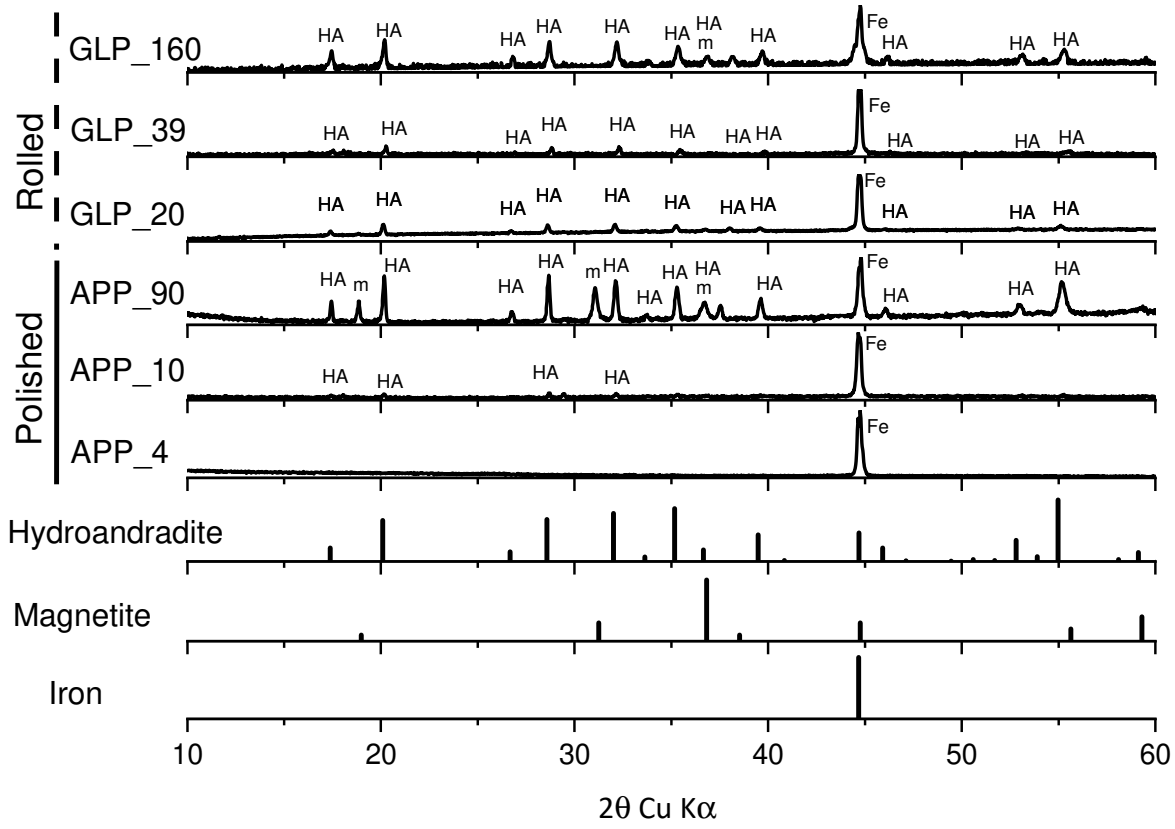

Figure 7. Evolution of XRD patterns for plate samples corroded in cementitious slurry. HA: hydroandradite. m: magnetite. Fe: ferrite.

3.2.2.3 μ-Raman spectroscopy

The μ-Raman spectrum collected on APP_4 displays two peaks at 541 and 666 cm^{-1} (Figure 8), which are diagnostic of magnetite (Fe_3O_4) [54]. Thus magnetite forms a thin film on the iron surface after four days of corrosion. The conditions of the study (i.e. alkaline medium and anoxic environment) are consistent with the formation of small-sized domains during the first growth phase of this oxide [28, 55]. The spectra for longer corrosion times (10 and 90 days) confirms the persistence of magnetite. However, new peaks at 318, 508, 864, 972 and 3615 cm^{-1} are detected, and are similar in position to the contributions observed for garnets such as andradite ($Ca_3Fe_2^{3+}(SiO_4)_4$) and grossular ($Ca_3Al_2(SiO_4)_4$) [56] as well as (hydro)andradite from Nagaland ophiolite [57]. The peak at 318 cm^{-1} can be attributed to vibration modes of silicate [58-60] in garnets, and specifically the groups bound to $Fe^{(III)}$ [58]. The peak at 508 cm^{-1} is explained by vibration of $Fe(OH)_6$ chemical bonds [61] which can be found in hydrogarnet. The peaks between 400 and 650 cm^{-1} are explained by bending of O-Si-O bonds [60, 62],

and the peaks at 864 and 972 cm^{-1} by stretching of Si-O bonds [60, 63]. The peak at 3615 cm^{-1} corresponds to stretching of hydroxide bonds (OH) [62, 64, 65] which are prevalent in the case of HA. The corrosion products observed for rolled plates are similar to those obtained for the polished substrates, meaning magnetite and HA could also be observed for these samples.

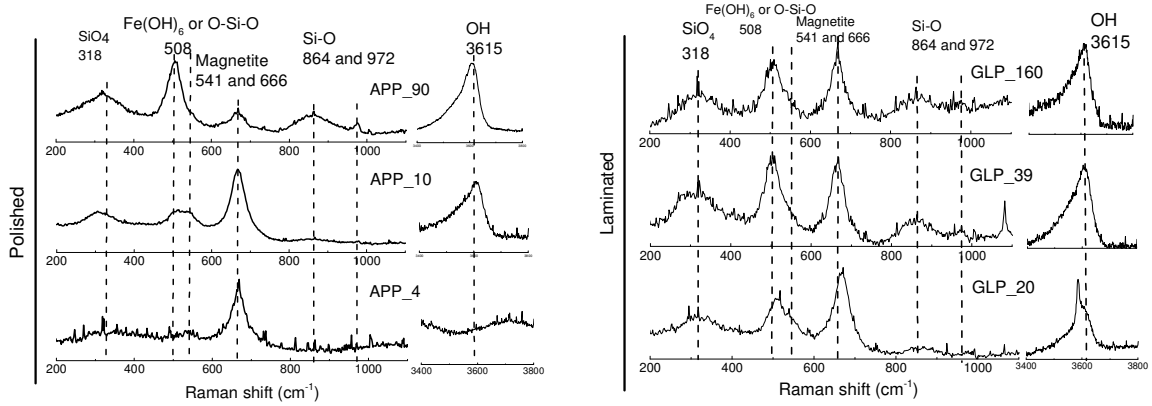

Figure 8. Evolution of µRaman spectra collected on polished and rolled plates as a function of reaction time in cementitious slurries.

3.2.2.4 Scanning Transmission electron microscopy

The corrosion interfaces are quite thin, posing significant challenge to a conventional cross-section analysis by SEM. To overcome this limitation, thin sections were extracted from the surface of reacted plates, and investigated by STEM and EDXS (Figure 9). Images and EDXS analysis for four days of reaction time (APP_4, Figure 9) confirm the presence of a thin (< 100 nm) layer enriched in O and Fe and covering the surface. The composition of this layer is consistent with an Fe (hydr)oxide, and corroborates the formation of magnetite. A few locations are also concentrated in Ca and Si, together with some Fe, which hints at the formation of HA-like compounds even for this short reaction time.

The corrosion interface observed for 10 days of reaction (APP_10) is notably distinct in terms of structural organization (Figure 9). The interfacial (Fe,O) (magnetite) layer is still present, but seems to be slightly thinner. It forms a median fringe which is partially covered by an outer layer of squat particles with an apparent diameter of ~1-2 µm. The chemical composition of these particles is dominated by O, Ca, Si, and Fe, meaning these solids probably correspond to HA. The fragmented nature of the outer layer parallels the SEM observations (Figure 4c), and confirms the absence of continuity for the

corrosion outer layer. The most notable feature, however, is the presence of jagged local voids with depths of up to 200 nm between the magnetite fringe and metal. Clearly these voids could not be observed by surface SEM, and they were too small to be reliably detected on conventional polished cross-sections. Note that some of these voids are gradually filled by HA precipitates. Finally, the metal surface seems to be covered by a thin (<100 nm) layer of (Fe,O) composition.

After 90 days of corrosion, STEM cross sections show that the outer HA particles have grown and coalesced, forming a continuous layer of 5-6 µm in thickness. The median fringe is still present, but significantly reduced in thickness. The iron surface is now significantly corrugated and heterogeneously corroded, with the thickness of corroded iron varying between 0 and up to 2 µm. Most of these cavities are filled either with HA, or with (Fe,O) solids (probably magnetite, the only Fe oxide detected for this sample). The STEM data also suggest, but do not offer definite proof for, the presence of an Fe oxide layer at the interface between metal and the corrosion products.

The interface observed for the rolled plate corroded over 160 days (GLP_160; Figure 10) is similar to that of APP_90. The outer layer of corrosion products is made of HA particles, and HA is also present as metal-replacing corrosion products, together with Fe oxide. The median fringe is also present, and an oxide layer is in contact with the highly jagged and corrugated metal surface. Interestingly, the corrosion layers are notably thinner than for the APP_90 sample. However, it is not clear whether this is due to difference in reactivity, or is simply due to some surface heterogeneities.

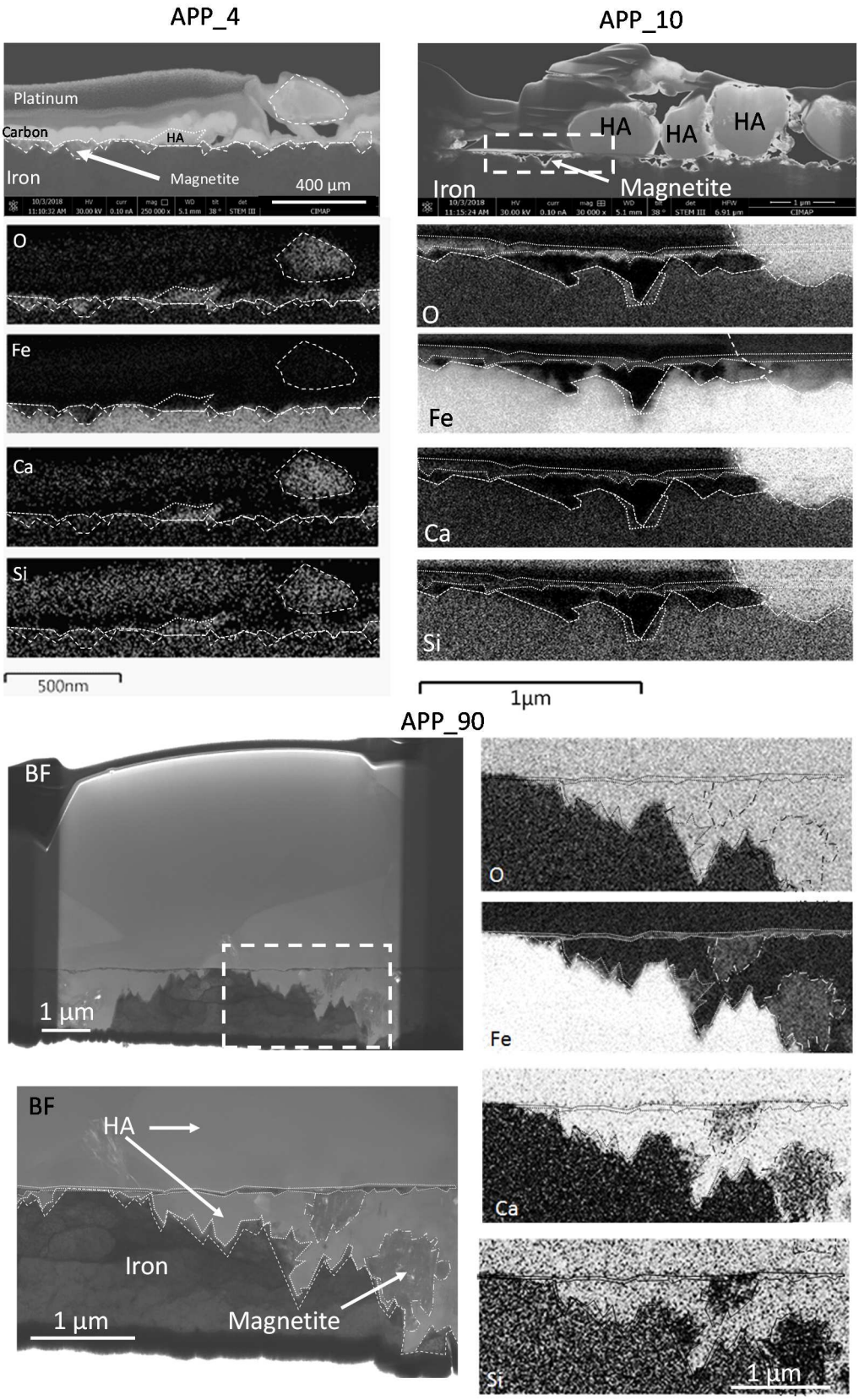

Figure 9. STEM pictures and EDXS element maps of the corrosion interface for iron polished plates samples immerged for 4, 10 and 90 days.

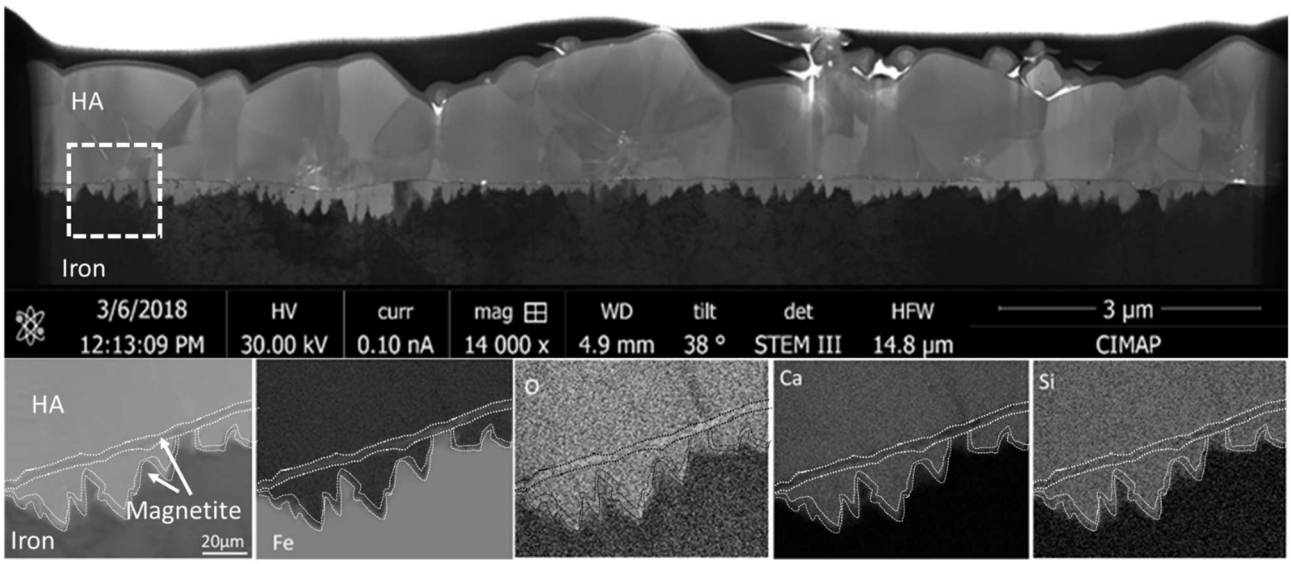

Figure 10. STEM picture (top) and EDXS element maps on the boxed area (bottom) of the corrosion interface for iron samples immerged for 160 days.

The oxidation state of Fe in the corrosion samples was further scrutinized by STXM [38]. This technique is based on the absorption of low-energy (soft) X-rays [40], and was used to collect maps of Fe $L_{2,3}$-edge X-ray absorption spectra over the corrosion interfaces. These spectra exhibit two distinct bands near 708 and 710 eV, the low- and high-energy contributions predominating for $Fe^{(II)}$ and $Fe^{(III)}$, respectively. In our case, this technique can be used to determine the Fe oxidation state in the layer and its stoichiometric distribution. Figure 11 shows the area on the FIB thin section for GLP_160 analyzed by STXM. The overall spectral hypermap is segmented in clusters of spectra with similar shapes.

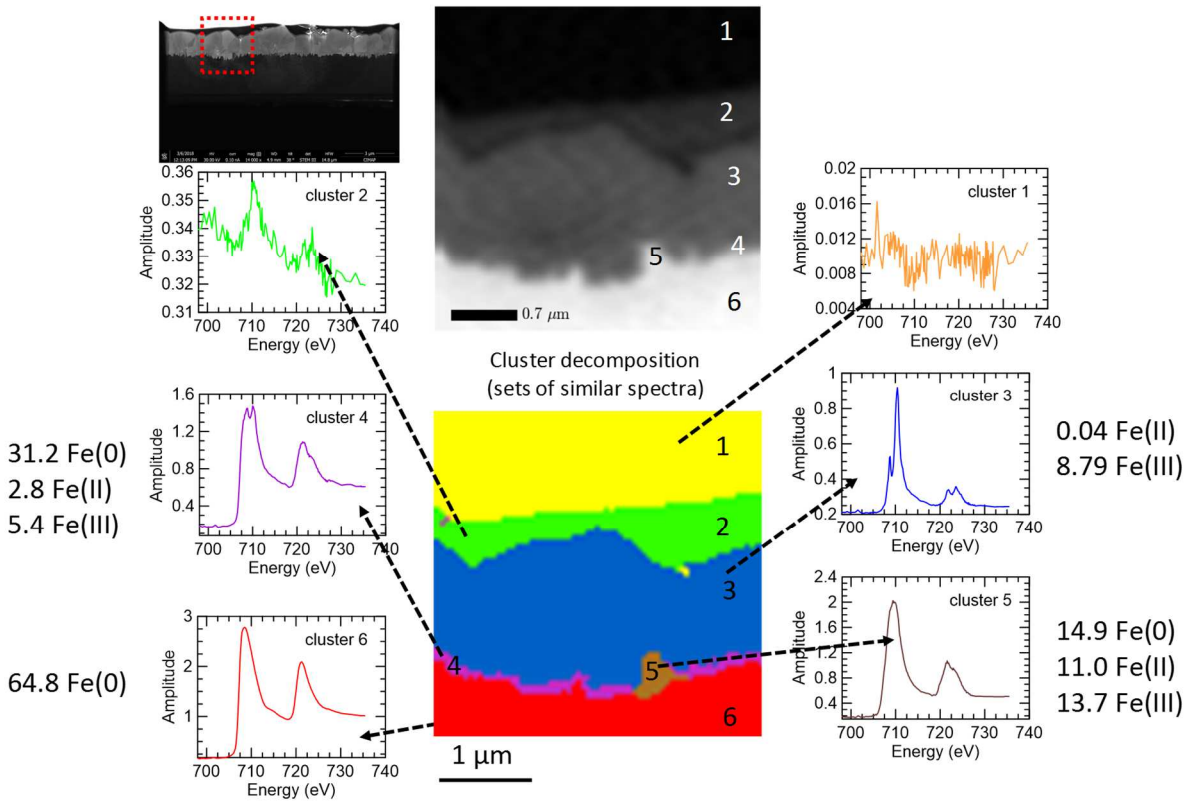

Figure 11. Mapping the areas of interest on the plates immersed for 160 days and the corresponding STXM results.

The median magnetite fringe is not observed on STXM maps. This is possibly because it is too thin compared to the overall lateral resolution of the STXM (30 nm) and would correspond to only 1 pixel width. Cluster 1 corresponds to the empty overspace while cluster 2 represents the protective platinum strip used during the preparation of the FIB thin section. Cluster 3 corresponds to the HA precipitates in the outer and metal-replacing layers. Spectral analysis indicate that the layers contain almost only $Fe^{(III)}$, consistent with the oxidation state of Fe in HA [45]. Clusters 5 and 6 correspond mostly to metal iron with a small contribution of oxidized Fe in cluster 5. Finally, the cluster decomposition singles out the oxide layer at the iron surface (cluster 4), and spectral decomposition indicates the presence of $Fe^{(0)}$ (due to nearby iron), $Fe^{(II)}$, and $Fe^{(III)}$. The $Fe^{(III)}/Fe^{(II)}$ ratio is close to 2, the value expected for magnetite. This layer has been detected in similar studies [38] and has been identified as a barrier layer [33].

4 Discussion

4.1 Impact of cement material on iron corrosion at 80°Ca

Our investigation demonstrates the role played both by the solution physico-chemical conditions and the presence of cement phases on the anoxic corrosion of iron in cementious systems at 80°C. Experiments with iron powder in absence of solid phases (porewater only) show the presence of an induction period of significant corrosion between 10 and 30 days, and of corrosion decrease within one month. This demonstrates that passivation rapidly occurs. In the presence of cement solids, the induction period shortens, total hydrogen evolution is greater, but passivation is attained more rapidly. The presence of cement solids also promotes the formation of hydroandradite, a phase which is not observed for experiments in cement-equilibrated filtered solution. This demonstrates that a steady supply of elements dissolved from solid sources is essential to precipitating hydrogarnet phases.

Characterization of plates reacted in a cement-containing slurry shows that the same phases (magnetite and hydroandradite) form as corrosion products. The corroded thickness is quite limited (less than 2 µm after about five months of corrosion), which points to an average corrosion rate smaller than 5 µm/year. The corrosion rate after a few months is expected to be even smaller, as the microscopic investigation clearly suggests that most of the iron corrosion occurred during the first months of interaction. Taken together, these results suggest that the presence of cement phases strongly influences corrosion thanks to the buffering of $[Ca]_{aq}$ and $[Si]_{aq}$. At the very beginning of the experiment, there is no dissolved Fe, but $[Fe]_{aq}$ steadily increases until supersaturation conditions are attained with respect to HA. These supersaturation conditions favor the formation of HA, first on the outer surface, meaning that the bare metal surface is not protected and dissolves rapidly. For the iron powder, the greater specific surface would imply a faster reactivity, leading to a greater short-term reaction, but to passivation after only 20 days. In contrast, for plates, corrosion stretches over a much longer time span of at least a few months. Eventually, HA precipitation in the inner voids results in the formation of a compact interface, favoring the creation of a barrier layer and limiting corrosion by thwarting diffusion of reacting dissolved species [66].

4.2 Corrosion mechanism

Our results show that the nature and the structure of the corrosion interface change with reaction time. Successive steps can be identified (Figure 12). The first phase of corrosion occurs just after iron immersion in solution and corresponds to the formation of a nm-scale layer of magnetite (Figure 12a). This initial formation of magnetite is a well-known phenomenon under anoxic aqueous conditions [16], and is usually explained by the oxidation of $Fe^{(0)}$ to $Fe^{(II)}$ to form $Fe(OH)_2$ [3, 67, 68]:

$$Fe + 2\,H_2O \rightarrow Fe(OH)_2 + H_2\uparrow \quad ,$$

followed by solid-state transformation of $Fe(OH)_2$ (also known as Schikorr reaction) [69]

$$3\,Fe(OH)_2 \rightarrow Fe_3O_4 + H_2\uparrow + 2H_2O$$

Another hypothesis for the formation of this magnetite layer invokes a solid-state reaction of coupled Fe diffusion toward the iron outer surface, and O diffusion toward the iron bulk, modeled as diffusion of O vacancies toward the surface [30, 33, 70, 71]. This reaction rate would then be controlled by the flux of vacancies toward the surface. A consequence of this solid-state reaction is that a fraction of Fe at the iron surface does not precipitate as magnetite, but is released as dissolved Fe. Under the alkaline conditions of the cement phase, the stable dissolved species would be $Fe(OH)_4^{2-}$, but the stability domain of this species in water is quite restricted [72]. This means that dissolved Fe would accumulate and possibly oxidize as $Fe(OH)_4^-$ until supersaturation with respect to HA is attained

The second step corresponds to nucleation and growth of HA crystallites at the iron outer surface, incorporating elements (mostly Ca and Si) released by cement dissolution [45, 73-76], according to

$$2\,Fe(OH)_4^- + 3\,Ca^{2+} + SiO(OH)_3^- + 3\,OH^- \rightarrow Ca_3Fe_2(SiO_4)(OH)_8 + 3H_2O$$

The formation of HA seems favored by the relatively high temperature conditions, as it forms only in small amounts at 20°C after three years of synthesis, but precipitates quantitatively at 110°C after only three days [45, 61]. This precipitation correlates with the formation of a layer of magnetite at the iron surface, probably corresponding to the oxido-reduction interface. This magnetite layer seems to grow along preferential zones, e.g. along defects or grain joints, thus leading to the observed jagged interface. Interestingly, the first magnetite layer does not disappear, but remains fairly stable (with, perhaps, a little dissolution over 160 days). Voids form between this fringe and the barrier layer. These voids probably

occur because Fe oxidized from the anodic reaction is readily incorporated by HA, thereby hindering the nucleation of any new phase. By maintaining relatively low $[Fe]_{aq}$, HA growth also hinders the growth of the barrier layer, and so maintains relatively high corrosion rates. This should result in the significant corrosion rate of the active dissolution stage, in which most of hydrogen evolution occurs for powders.

The third step corresponds to the growth of HA particles in the outer layer and in the metal-replacing voids, eventually forming a metal-replacing layer of corrosion products. This continuous layer of corrosion products limits the flux of reactants and products and significantly alters the limiting conditions at the surface of the barrier layer. As a consequence, the diffusion reaction within the barrier layer significantly slows down. The thin magnetite fringe directly at the iron surface would itself possibly correspond to the barrier layer [30, 31, 33]. The combination of this protecting barrier layer and diffusion-limiting HA layer would eventually slow down the corrosion rate, explaining why, after almost six months of reaction at 80°C, corrosion penetration is only about 2 µm.

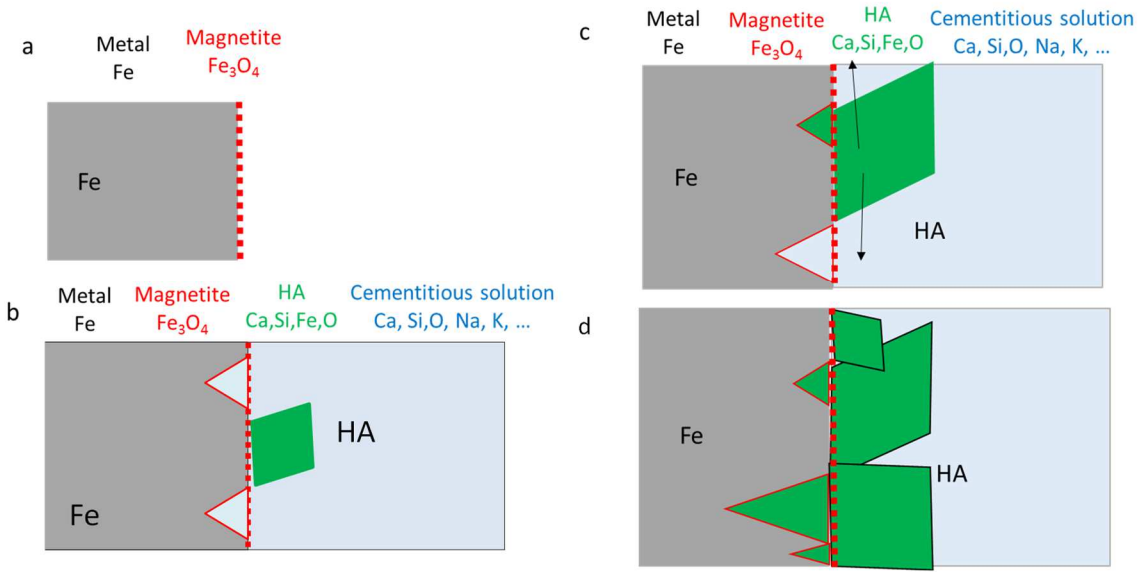

Figure 12. Schematic representation of iron-cement solution corrosion interface for (a) formation of magnetite during the first step, (b and c) growth of HA and formation of voids replacing metal. (d) Precipitation of HA within the metal-replacing voids.

4.3 Estimation of the amount of corrosion

The amount of corroded iron can be assessed first from the volume of evolved H_2, provided the stoichiometry of oxido-reduction reaction is known. Under our anoxic conditions, the coupled reactions between Fe oxidation and water reduction simply write

$$Fe + 2\,H_2O \rightarrow Fe^{2+} + 2OH^- + H_2\uparrow$$

and

$$Fe + 3\,H_2O \rightarrow Fe^{3+} + 3OH^- + 3/2\,H_2\uparrow$$

For Fe final oxidation states of +II and + III, respectively. A rapid calculation shows that, depending on the final oxidation state of Fe, 86 and 21 wt.% of iron is oxidized at the end of the GPC and GPWoutC experiments, respectively. The amount of corroded iron for the plate samples is much more limited (0.36 wt.% for AAP_90).

Oxidized Fe can be retained in the corrosion products, or, alternatively, dissolved and get transported away from the interface [34, 77]. The magnitude of the possible Fe loss can be obtained by comparing the thickness of corroded iron and the amount of oxidized Fe retained in the corrosion products. The amount of Fe in corrosion products is conveniently assessed by the equivalent thickness e_{eq} of metal iron. This value is calculated from the fraction of Fe present in each homogeneous corrosion layer as [34, 78, 79]

$$e_{eq} = \sum_i d_i F_i \frac{\rho_i}{\rho_{Fe}}$$

where d_i, ρ_i and F_i are is the thickness, density and mass fraction of Fe for each corrosion layer i, ρ_{Fe} is the density of metal iron, and the sum runs over all corrosion layers at the interface. To simplify, the outer layer and HA-containing metal-replacing layers were assumed to be made of HA only, with no porosity. The median fringe and the metal-contacting barrier layer were assumed to be made of magnetite only. The density for HA and magnetite were taken equal to $\rho_{HA} = 3.13$ [46] and $\rho_{magnetite} = 5.2$ [34]. The e_{eq} calculations are summarized in Table 6. The final e_{eq} value (0.16 µm) is somewhat smaller than the thickness of corroded iron, obtained by adding the thicknesses of the barrier layer and

468 the metal-replacing layer, i.e. 0.03 + 0.22 = 0.25 µm. This suggests that a significant fraction of Fe must
469 dissolve away from the interface.

Table 6. Parameters and values for the calculation of e_{eq}.

Unit	Composition	F_i[a]	ρ_i[b]	APP_90		GLP_160	
				d_i[c] (µm)	e_{eq}[d] (µm)	d_i (µm)	e_{eq} (µm)
Barrier layer	magnetite	0.72	5.2	0.09	0.043	0.03	0.014
Metal-replacing layer	HA[a]	0.23	3.16	1.4	0.13	0.22	0.02
Median fringe	magnetite	0.72	5.2	0.03	0.014	0.028	0.014
Outer layer	HA	0.23	3.16	4.0	0.37	1.13	0.11
Total					**0.56**		**0.16**

[a] mass fraction of Fe in layer i
[b] density of layer i
[c] thickness of layer i
[d] equivalent thickness of layer i
[e] Hydroandradite

470

471 # 5 Conclusions

472 Corrosion studies on iron under anoxic cementious conditions highlight the role played by both solution
473 composition and iron corrosion in the nature of corrosion products. The initial layer of magnetite
474 indicates that corrosion is initially driven solely by electrochemical reactions at the iron surface. The
475 next step of voids forming at the iron surface coupled with HA precipitation on the outer surfaces
476 emphasizes the role played by precipitation reactions in maintaining relatively high initial rates of
477 corrosion. This explains the initial acceleration of corrosion in presence of cement phases. Eventually,
478 these precipitates cover the interface, fill the voids and limit the transport of reactants and species, which
479 results in slower corrosion. Thus, simple experiments performed after a couple of days would not capture
480 this complex behavior

481 Another interesting point is the detection of successive layers of HA and magnetite. Our time-resolved
482 study has pinpointed the origin of each of these layers, and provides a reasonable explanation for this
483 succession. A tentative explanation based on a single structural observation after more than three months
484 would have been comparatively more complicated, and would not have been able to explain the non-
485 linear variations in Fe oxidation.

Finally, our study also demonstrates the key role played by the barrier layer in controlling the corrosion rate and long term protection/passivation of carbon steel in anoxic environments. Previous studies in soil and clay systems have indeed demonstrated that this layer is a key to corrosion limitation [38]. In fact, this layer is a common feature for experiments demonstrating long-term inhibition of corrosion under anoxic conditions, whether in carbonate system [39], in clay [38], or in cement phase (this study). It supports our case that it is this layer which is responsible first for the limitation of carbon steel corrosion under anoxic conditions. Clearly, the formation of this passive layer is anticipated in the conditions of the Belgian supercontainer for radioactive waste disposal. Therefore, iron corrosion should be maintained at a value low enough to guarantee the long-term integrity of the overpack before it is eventually exposed to the clay porewater.

5.1 Acknowledgements

The authors acknowledge the financial support provided by CEA and ONDRAF/NIRAS (Contract CEA-ONDRAF DRF/DCEPI/CJ2016-477). Bernard Grenut (deceased) is thanked for his assistance in sample preparation, Stéphane Poyet for the chemical and mineralogical characterization of the CEM I, Emmanuel Gardès and Delphine Marie Levavasseur (CIMAP-GANIL, Caen) for FIB-STEM-EDXS preparations and analyses, Isabelle Monet (CIMAP-GANIL, Caen) for TEM experiment and Barbara Lothenbach for ICSD 29247 of hydroandradite. James J. Dynes and the SM beamline staff are thanked for their assistance during data acquisition, and the CLS for provision of beamtime. The CLS is supported by NSERC, CIHR, NRC, the Province of Saskatchewan, WEDC and the University of Saskatchewan. We thank Oscar Mattos for his editorialship, and three anonymous reviewers for fruitful comments on the manuscript.

Data Availability

The raw/processed data required to reproduce these findings cannot be shared at this time due to legal reasons.

Contrat :

Contrat CEA-ONDRAF
DRF/DCEPI/CJ2016-477
CCHO 2016-0671/00/00

EOTP

A-COSTO-02-10

6 References

[1] B. Kursten, F. Druyts, D.D. Macdonald, N.R. Smart, R. Gens, L. Wang, E. Weetjens, J. Govaerts, Review of corrosion studies of metallic barrier in geological disposal conditions with respect to Belgian Supercontainer concept, Energy Mater., 6 (2011) 91-97.

[2] B. Kursten, F. Druyts, Methodology to make a robust estimation of the carbon steel overpack lifetime with respect to the Belgian Supercontainer design, J. Nucl. Mater., 379 (2008) 91-96.

[3] N.R. Smart, A.P. Rance, P.A.H. Fennell, B. Kursten, Effect of sulphur species on anaerobic corrosion of carbon steel in alkaline media, Corr. Eng. Sci. Technol., 49 (2014) 473-479.

[4] P. Ghods, O. Burkan Isgor, F. Bensebaa, D. Kingston, Angle-resolved XPS study of carbon steel passivity and chloride-induced depassivation in simulated concrete pore solution, Corr. Sci., 58 (2012) 159-167.

[5] P. Ghods, O.B. Isgor, G. McRae, T. Miller, The effect of concrete pore solution composition on the quality of passive oxide films on black steel reinforcement, Cem. Concr. Comp., 31 (2009) 2-11.

[6] M.K. Nieuwoudt, J.D. Comins, I. Cukrowski, The growth of the passive film on iron in 0.05 M NaOH studied *in situ* by Raman micro-spectroscopy and electrochemical polarisation. Part I: near-resonance enhancement of the Raman spectra of iron oxide and oxyhydroxide compounds, J. Raman Spectrosc., 42 (2011) 1335-1339.

[7] M.K. Nieuwoudt, J.D. Comins, I. Cukrowski, The growth of the passive film on iron in 0.05 M NaOH studied *in situ* by Raman microspectroscopy and electrochemical polarization. Part II: In situ Raman spectra of the passive film surface during growth by electrochemical polarization, J. Raman Spectrosc., 42 (2011) 1353-1365.

[8] M.K. Nieuwoudt, J.D. Comins, I. Cukrowski, Analysis of the composition of the passive film on iron under pitting conditions in 0.05 M NaOH/NaCl using Raman microscopy in situ with anodic polarisation and MCR-ALS, J. Raman Spectrosc., 43 (2012) 928-938.

547 [9] L. Chomat, V. L'Hostis, E. Amblard, L. Bellot-Gurlet, Long term study of passive corrosion of steel
548 rebars in Portland mortar in context of nuclear waste disposal, Corr. Eng. Sci. Technol., 49 (2014) 467-
549 472.

550 [10] V. L'Hostis, E. Amblard, C. Blanc, F. Miserque, C. Paris, L. Bellot-Gurlet, Passive corrosion of
551 steel in concrete in context of nuclear waste disposal, Corr. Eng. Sci. Technol., 46 (2011) 177-181.

552 [11] J.M. Deus, B. Diaz, L. Freire, X.R. Novoa, The electrochemical behaviour of steel rebars in
553 concrete: an Electrochemical Impedance Spectroscopy study of the effect of temperature, Electrochim.
554 Acta, 131 (2014) 106-115.

555 [12] C. Andrade, M. Keddam, X.R. Nóvoa, M.C. Pérez, C.M. Rangel, H. Takenouti, Electrochemical
556 behaviour of steel rebars in concrete: influence of environmental factors and cement chemistry,
557 Electrochim. Acta, 46 (2001) 3905-3912.

558 [13] C. Andrade, P. Merino, X.R. Nóvoa, M.C. Pérez, L. Soler, Passivation of Reinforcing Steel in
559 Concrete, Mater. Sci. Forum, 192-194 (1995) 891-898.

560 [14] B. Huet, V. L'Hostis, F. Miserque, H. Idrissi, Electrochemical behavior of mild steel in concrete:
561 Influence of pH and carbonate content of concrete pore solution, Electrochim. Acta, 51 (2005) 172-180.

562 [15] R.M. Ghantous, S. Poyet, V. L'Hostis, N.-C. Tran, R. François, Effect of crack openings on
563 carbonation-induced corrosion, Cem. Concr. Res., 95 (2017) 257-269.

564 [16] W. López, J.A. González, Influence of the degree of pore saturation on the resistivity of concrete
565 and the corrosion rate of steel reinforcement, Cem. Concr. Res., 23 (1993) 368-376.

566 [17] N. Senior, R. Newman, S. Wang, N. Diomidis, Understanding and quantifying the anoxic corrosion
567 of carbon steel in a Swiss L/ILW repository environment, Corr. Eng. Sci. Technol., 52 (2017) 78-83.

568 [18] X. He, T. Ahn, J.-P. Gwo, Carbon Steel Corrosion in Simulated Anoxic Concrete Pore Water for
569 Nuclear Waste Disposal Application, Corrosion, 73 (2017) 1381-1393.

570 [19] B. Li, Y. Huan, Zhang, Passivation and Corrosion Behavior of P355 Carbon Steel in Simulated
571 Concrete Pore Solution at pH 12.5 to 14, Int. J. Electrochem. Sci., (2017) 10402-10420.

572 [20] P. Lu, S. Sharifi-Asl, B. Kursten, D.D. Macdonald, The Irreversibility of the Passive State of
573 Carbon Steel in the Alkaline Concrete Pore Solution under Simulated Anoxic Conditions, J.
574 Electrochem. Soc., 162 (2015) C572-C581.

575 [21] P. Ghods, O.B. Isgor, J.R. Brown, F. Bensebaa, D. Kingston, XPS depth profiling study on the
576 passive oxide film of carbon steel in saturated calcium hydroxide solution and the effect of chloride on
577 the film properties, Appl. Surf. Sci., 257 (2011) 4669-4677.

578 [22] G. Blanco, A. Bautista, H. Takenouti, EIS study of passivation of austenitic and duplex stainless
579 steels reinforcements in simulated pore solutions, Cem. Concr. Comp., 28 (2006) 212-219.

580 [23] C. Monticelli, A. Frignani, G. Trabanelli, A study on corrosion inhibitors for concrete application,
581 Cem. Concr. Res., 30 (2000) 635-642.

582 [24] H. Luo, H. Su, C. Dong, K. Xiao, X. Li, Electrochemical and passivation behavior investigation of
583 ferritic stainless steel in simulated concrete pore media, Data in Brief, 5 (2015) 171-178.

584 [25] M. Saremi, E. Mahallati, A study on chloride-induced depassivation of mild steel in simulated
585 concrete pore solution, Cem. Concr. Res., 32 (2002) 1915-1921.

586 [26] X.-H. Sun, X.-B. Zuo, G.-J. Yin, K. Jiang, Y.-J. Tang, Electrochemical and microscopic
587 investigation on passive behavior of ductile iron in simulated cement-mortar pore solution, Construct.
588 Build. Mater., 150 (2017) 703-713.

589 [27] S. Chakri, P. David, I. Frateur, A. Galtayries, P. Marcus, E. Sutter, B. Tribollet, V. Vivier, S. Zanna,
590 Effet de la composition chimique de la solution interstitielle de bétons jeunes sur la passivation d'un
591 acier doux, Matériaux & Techniques, 103 (2015) 209.

592 [28] J.M. Gras, La corrosion generalisée des aciers au carbone dans l'eau à haute temperature, EDF,
593 Électricité de France, 1995.

594 [29] F.H. Sweeton, C.F. Baes, The solubility of magnetite and hydrolysis of ferrous ion in aqueous
595 solutions at elevated temperatures, J. Chem. Thermodyn., 2 (1970) 479-500.

596 [30] C.Y. Chao, L.F. Lin, D.D. Macdonald, A Point Defect Model for Anodic Passive Films I . Film
597 Growth Kinetics, J. Electrochem. Soc., 128 (1981) 1187-1194.

598 [31] L.F. Lin, C.Y. Chao, D.D. Macdonald, A Point Defect Model for Anodic Passive Films. 2.
599 Chemical Breackdown and Pit Initiation, J. Electrochem. Soc., 128 (1981) 1194-1198.

600 [32] M. Bojinov, G. Fabricius, T. Laitinen, K. Mäkelä, T. Saario, G. Sundholm, Coupling between ionic
601 defect structure and electronic conduction in passive films on iron, chromium and iron–chromium
602 alloys, Electrochim. Acta, 45 (2000) 2029-2048.

603 [33] C. Bataillon, F. Bouchon, C. Chainais-Hillairet, C. Desgranges, E. Hoarau, F. Martin, S. Perrin, M.
604 Tupin, J. Talandier, Corrosion modelling of iron based alloy in nuclear waste repository, Electrochim.
605 Acta, 55 (2010) 4451-4467.

606 [34] M.L. Schlegel, C. Bataillon, K. Benhamida, C. Blanc, D. Menut, J.-L. Lacour, Metal corrosion and
607 argillite transformation at the water-saturated, high-temperature iron–clay interface: A microscopic-
608 scale study, Appl. Geochem., 23 (2008) 2619-2633.

609 [35] D. Neff, S. Reguer, L. Bellot-Gurlet, P. Dillmann, R. Bertholon, Structural characterization of
610 corrosion products on archaeological iron: an integrated analytical approach to establish corrosion
611 forms, J. Raman Spectrosc., 35 (2004) 739-745.

612 [36] P.J. Heaney, E.P. Vicenzi, L.A. Gianuzzi, K.J.T. Livi, Focused ion beam milling: a method of site-
613 specific sample extraction for microanalysis of Earth and planetary materials, Am. Miner., 86 (2001)
614 1094-1099.

615 [37] K.V. Kaznatcheev, C. Karunakaran, U.D. Lanke, S.G. Urquhart, M. Obst, A.P. Hitchcock, Soft X-
616 ray spectromicroscopy beamline at the CLS: Commissioning results, Nucl. Instr. Meth. Phys. Res. A,
617 582 (2007) 96-99.

618 [38] Y. Leon, P. Dillmann, D. Neff, M.L. Schlegel, E. Foy, J.J. Dynes, Interfacial layers at a nanometre
619 scale on iron corroded in carbonated anoxic environments, RSC Adv., 7 (2017) 20101-20115.

620 [39] Y. Leon, M. Saheb, E. Drouet, D. Neff, E. Foy, E. Leroy, J.J. Dynes, P. Dillmann, Interfacial layer
621 on archaeological mild steel corroded in carbonated anoxic environments studied with coupled micro
622 and nano probes, Corros. Sci., 88 (2014) 23-35.

623 [40] A. Michelin, E. Drouet, E. Foy, J. J. Dynes, D. Neff, P. Dillmann, Investigation at the nanometre
624 scale on the corrosion mechanisms of archaeological ferrous artefacts by STXM, J. Anal. Atom.
625 Spectrom., 28 (2013) 59-66.

626 [41] J. Stöhr, NEXAFS spectroscopy, Springer-Verlag, Berlin, 1992.

627 [42] J.J. Dynes, T. Tyliszczak, T. Araki, J.R. Lawrence, G.D.W. Swerhone, G.G. Leppard, A.P.
628 Hitchcock, Speciation and quantitative mapping of metal species in microbial biofilms using scanning
629 transmission X-ray microscopy, Environ. Sci. Technol., 40 (2006) 1556-1565.

630 [43] A. Michelin, E. Drouet, E. Foy, J.J. Dynes, D. Neff, P. Dillmann, Investigation at the nanometre
631 scale on the corrosion mechanisms of archaeological ferrous artefacts by STXM, J. Anal. At. Spectrom.,
632 28 (2013) 59-66.

633 [44] R. Zhang, S. Zheng, S. Ma, Y. Zhang, Recovery of alumina and alkali in Bayer red mud by the
634 formation of andradite-grossular hydrogarnet in hydrothermal process, J. Hazard. Mater., 189 (2011)
635 827-835.

636 [45] B.Z. Dilnesa, B. Lothenbach, G. Renaudin, A. Wichser, D. Kulik, Synthesis and characterization
637 of hydrogarnet $Ca_3(Al_xFe_{1-x})_2(SiO_4)_y(OH)_{4(3-y)}$, Cem. Concr. Res., 59 (2014) 96-111.

638 [46] C. Cohen-Addad, Étude du Composé $Ca_3Fe_2(SiO_4)_{1.15}(OH)_{7.4}$ par Absorption Infrarouge et
639 Diffraction des Rayons X et des Neutrons, Acta Cryst. A, 26 (1970) 68-70.

640 [47] A. Carnot, I. Frateur, S. Zanna, B. Tribollet, I. Dubois-Brugger, P. Marcus, Corrosion mechanisms
641 of steel concrete moulds in contact with a demoulding agent studied by EIS and XPS, Corr. Sci., 45
642 (2003) 2513-2524.

643 [48] R.P. Gupta, S.K. Sen, Calculation of multiplet structure of core p-vacancy levels, Phys. Rev. B, 10
644 (1974) 71.

[49] R.P. Gupta, S.K. Sen, Calculation of multiplet structure of core p-vacancy levels. II, Phys. Rev. B, 12 (1975) 15.

[50] A.P. Grosvenor, B.A. Kobe, M.C. Biesinger, N.S. McIntyre, Investigation of multiplet splitting of Fe 2p XPS spectra and bonding in iron compounds, Surf. Interf. Anal., 36 (2004) 1564-1574.

[51] R. D'Angelo, M. Roy, T. Pauporté, S. Delaunay, D. You, C. Mansour, F. Miserque, F. Foct, Study of the effect of polyacrylic acid dispersant on magnetite deposits in steam generators conditions, Mater. Chem. Phys., 226 (2019) 118-128.

[52] H. Seyama, M. Soma, Fe 2p spectra of silicate minerals, J. Electron Spectr. Rel. Phen., 42 (1987) 97–101.

[53] R.D. Desautels, M.P. Rowe, M. Jones, A. Whallen, J. van Lierop, Spontaneously Formed Interfacial Metal Silicates and Their Effect on the Magnetism of Superparamagnetic FeCo/SiO2 Core/Shell Nanoparticles, Langmuir, 31 (2015) 2879-2884.

[54] O.N. Shebanova, P. Lazor, Raman spectroscopic study of magnetite ($FeFe_2O_4$): a new assignment for the vibrational spectrum, J. Solid State Chem., 174 (2003) 424-430.

[55] J.E. Castel, G.M.W. Mann, The mechanism of formation of porous oxide film, Corr. Sci., 6 (1966) 253-262.

[56] A.M. Hofmeister, A. Chopelas, Vibrational spectroscopy of end-member silicate garnets, Phys. Chem. Miner., 17 (1991) 503-526.

[57] B. Ghosh, T. Morishita, J. Ray, A. Tamura, T. Mizukami, Y. Soda, T.N. Ovung, A new occurrence of titanian (hydro)andradite from the Nagaland ophiolite, India: Implications for element mobility in hydrothermal environments, Chem. Geol., 457 (2017) 47-60.

[58] A.M. Hofmeister, A. Chopelas, Vibrational spectroscopy of end-member silicate garnets, Phys. Chem. Miner., 17 (1991) 503–526.

[59] B.A. Kolesov, C.A. Geiger, Raman scattering in silicate garnets: an investigation of their resonance intensities, J. Raman Spectrosc., 28 (1997) 659-662.

[60] D. Bersani, S. Andò, P. Vignola, G. Moltifiori, I.-G. Marino, P.P. Lottici, V. Diella, Micro-Raman spectroscopy as a routine tool for garnet analysis, Spectrochim. Acta A, 73 (2009) 484-491.

[61] B.Z. Dilnesa, Fe-containing hydrates and their fate during cement hydration: thermodynamic data and experimental study, (2011), PhD Thesis, Ecole Polytechnique fédérale de Lausanne (Switzerland).

[62] D.C. Smith, A review of the non-destructive identification of diverse geomaterials in the cultural heritage using different configurations of Raman spectroscopy, Geological Society, London, Special Publications, 257 (2006) 9-32.

[63] A. Friedrich, B. Winkler, W. Morgenroth, A. Perlov, V. Milman, Pressure-induced spin collapse of octahedrally coordinated Mn^{3+} in the tetragonal hydrogarnet henritermierite $Ca_3Mn_2[SiO_4]_2[O_4H_4]$, Phys. Rev. B, 92 (2015).

[64] A. Wang, J.J. Freeman, B.L. Jolliff, Understanding the Raman spectral features of phyllosilicates, J. Raman Spectrosc., 46 (2015) 829-845.

[65] M. Dulski, K.M. Marzec, J. Kusz, I. Galuskina, K. Majzner, E. Galuskin, Different route of hydroxide incorporation and thermal stability of new type of water clathrate: X-ray single crystal and Raman investigation, Sci. Rep., 7 (2017) 9046.

[66] S. Nešić, M. Nordsveen, R. Nyborg, A. Stangeland, A mechanistic model for carbon dioxide corrosion of mild steel in the presence of protective iron carbonate films - Part 2: A numerical experiment, Corrosion, 59 (2003) 489-497.

[67] N.R. Smart, A.P. Rance, P.A.H. Fennell, B. Kursten, The anaerobic corrosion of carbon steel in alkaline media – Phase 2 results, EPJ Web of Conferences, 56 (2013) 06003.

[68] N.R. Smart, A.P. Rance, D.J. Nixon, P.A.H. Fennell, B. Reddy, B. Kursten, Summary of studies on the anaerobic corrosion of carbon steel in alkaline media in support of the Belgian supercontainer concept, Corr. Eng. Sci. Technol., 52 (2017) 217-226.

[69] G. Schikorr, Über Eisen(II)-hydroxyd und ein ferromagnetisches Eisen(III)-hydroxyd, Zeit. Anorg. Allg. Chem., 212 (1933) 33-39.

[70] D.D. Macdonald, M. Urquidi-Macdonald, Theory of Steady-State Passive Films, J. Electrochem. Soc., 137 (1990) 2395-2402.

[71] D.D. Macdonald, The point defect model for the passive state, 1992.

[72] J. Chivot, Thermodynamique des produits de corrosion. Fonctions thermodynamiques, diagrammes de solubilité, diagrammes E-pH des systèmes Fe-H_2O, Fe-CO_2-H_2O, Fe-S-H_2O, Cr-H_2O et Ni-H_2O en fonction de la temperature, ANDRA, Châtenay-Malabry, France, 2004.

[73] C. Rios, C. Williams, M. Fullen, Hydrothermal synthesis of hydrogarnet and tobermorite at 175 °C from kaolinite and metakaolinite in the CaO–Al_2O_3–SiO_2–H_2O system: A comparative study, Appl. Clay Sci., 43 (2009) 228-237.

[74] P. Adhikari, C.C. Dharmawardhana, W.-Y. Ching, Structure and properties of hydrogrossular mineral series, J. Amer. Ceram. Soc., 100 (2017) 4317-4330.

[75] K. Kyritsis, N. Meller, C. Hall, Chemistry and Morphology of Hydrogarnets Formed in Cement-Based CASH Hydroceramics Cured at 200° to 350°C, J. Amer. Ceram. Soc., 92 (2009) 1105-1111.

[76] E. Passaglia, R. Rinaldi, Katoite, a new member of the $Ca_3Al_2(SiO_4)_3$-$Ca_3Al_2(OH)_{12}$ series and a new nomenclature for the hydrogrossular group of minerals, Bull. Minéral., 107 (1984) 605-618.

[77] M.L. Schlegel, C. Bataillon, F. Brucker, C. Blanc, D. Prêt, E. Foy, M. Chorro, Corrosion of metal iron in contact with anoxic clay at 90 °C: Characterization of the corrosion products after two years of interaction, Appl. Geochem., 51 (2014) 1-14.

[78] W.-J. Chitty, P. Dillmann, V. L'Hostis, C. Lombard, Long-term corrosion resistance of metallic reinforcements in concrete—a study of corrosion mechanisms based on archaeological artefacts, Corr. Sci., 47 (2005) 1555-1581.

[79] M.L. Schlegel, C. Bataillon, C. Blanc, D. Prêt, E. Foy, Anodic activation of iron corrosion in clay media under water-saturated conditions at 90 C: characterization of the corrosion interface, Environ. Sci. Technol., 44 (2010) 1503–1508.